Synthesis and Crystallization of Atomic Layer Deposition β-Eucryptite $LiAlSiO_4$ Thin-Film Solid Electrolytes

Ryan Sheil,[‖] Ya-Chuan Perng,[‖] Julian Mars, Jea Cho, Bruce Dunn, Michael F. Toney, and Jane P. Chang*

ABSTRACT: Atomic layer deposition (ALD) was used to control the stoichiometry of thin lithium aluminosilicate films, thereby enabling crystallization into the ion-conducting β-eucryptite $LiAlSiO_4$ phase. The rapid thermal annealed ALD film developed a well-defined epitaxial relationship to the silicon substrate: β-$LiAlSiO_4$ $(1\bar{2}10)$||Si (100) and β-$LiAlSiO_4$ $(10\bar{1}0)$||Si (001). The extrapolated room temperature ionic conductivity was found to be 1.2×10^{-7} S/cm in the $[1\bar{2}10]$ direction. Because of the unique 1-D channel along the c axis of β-$LiAlSiO_4$, the epitaxial thin film has the potential to facilitate ionic transport if oriented with the c axis normal to the electrode surface, making it a promising electrolyte material for three-dimensional lithium-ion microbatteries.

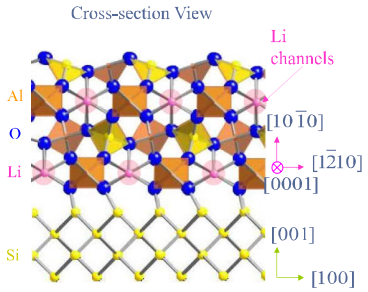

KEYWORDS: *crystalline solid electrolyte, atomic layer deposition, thin-film processing, 3D batteries, lithium-ion batteries, epitaxial thin films*

■ INTRODUCTION

Lithium-ion batteries are the premier power source for a wide range of mobile electronic devices as well as electric vehicles. In the era of internet of things where a trillion sensors are projected to be needed each year to support autonomous operation in sensing, actuation, and communication, lithium-ion batteries are an excellent candidate to power these small-scale devices.[1] Miniaturization of lithium-ion batteries has been successfully implanted as a planar stack of solid-state thin-film components but suffers from low areal energy densities because of limited film thicknesses. In this 2D design, the thicknesses of the electrodes are limited by poor Li^+ transport (as well as mechanical considerations), which creates limited areal loading. A transition to three-dimensional (3D) architectures has gained much recent attention, because of its ability to mitigate some of the trade-offs between areal energy and power density through increased surface area to volume ratios of the electrode materials—producing improved efficiency in electrode material loading per area. Several 3D battery designs have been proposed, including interdigitated pillars, concentric tubes, aperiodic sponges, and trenches.[2,3] Each of these 3D designs involves a nonplanar electrode structure and requires a conformal coating of the solid electrolyte over the electrode—making atomic layer deposition (ALD) an excellent synthesis technique because of its non-line-of-sight nature.[3−6]

The three main requirements for a solid electrolyte of this type are high ionic conductivity, low electrical conductivity, and thickness uniformity.[7,8] Various techniques have been employed to deposit lithium-containing thin films, including pulsed laser deposition, e-beam evaporation, sol−gel deposition, chemical vapor deposition, magnetron sputtering, and ALD.[9−17] Atomic layer deposition as a gas-phase synthesis technique offers the unique advantage of conformal deposition across high aspect ratio structures but with the drawback of slow growth rates. In the case of the solid electrolyte, this drawback is somewhat mitigated in that the diffusion time for Li^+ across the electrolyte layer scales with the square of the thickness, meaning thinner layers lead to lower ohmic losses as long as the layer is thick enough to resist breakdown and excessive leakage current. In this accord, ALD has been utilized to successfully synthesize a wide range of thin-film solid electrolyte materials,[14,18−25] in addition to anodes,[6,26−31] cathodes,[32−35] barriers,[7] and current collectors[36−39] as well as 3D batteries consisting of all atomic layer deposited materials on a Si trench structure.[7]

Although many oxide-based solid electrolytes have been synthesized via ALD to date, they generally exhibit much lower ionic conductivities as compared to their crystalline counterparts because of their specific structural arrangement that facilitates fast lithium-ion transport. In the ALD synthesis of Al-doped $Li_7La_3Zr_2O_{12}$—a promising solid-state electrolyte

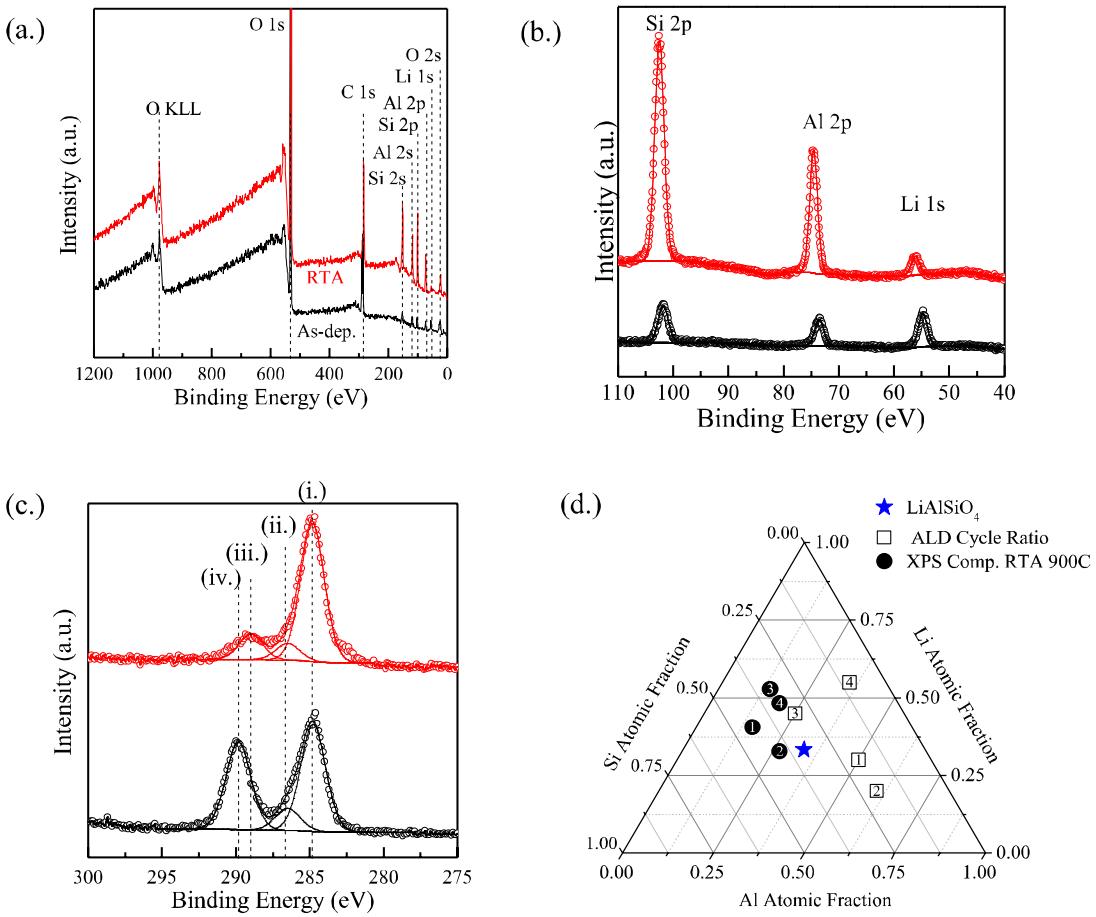

Figure 1. (a) XPS survey spectra of a $Li_xAl_ySi_zO$ thin film deposited via the ALD cycle sequence $[12(Al_2O_3)\text{-}4(LiOH)\text{-}4(SiO_2)]x5$ corresponding to a ∼17 nm thickness. High-resolution XPS detailed scans showing the Li 1s, Al 2p, Si 2p, and C 1s in the panels *b* and *c*, respectively, where the spectra corresponding to the as-deposited thin film are shown in black and post RTA treatment in red. The as-deposited film was found to be lithium-rich most likely because of surface driven diffusion and reaction to form lithium carbonate as seen in (c) with the C 1s peak at 290 eV (iv). Carbon 1s peaks are shown in panel c in which (i) corresponds to sp^3 carbon−carbon bonding, (ii) to carbon−oxygen binding, (iii) to carbon−oxygen double bond, and (iv) to carbonate. (d) Tertiary diagram of various $Li_xAl_ySi_zO$ samples deposited utilizing the ALD cycle sequence $a(Al_2O_3)\text{-}b(LiOH)\text{-}c(SiO_2)$. The ALD cycle ratios are shown as squares, whereas the XPS-determined compositions post RTA are shown as circles.

with ionic conductivities as high as 10^{-3} S/cm at room temperature,[24] the stoichiometry of the as-deposited films could be finely controlled; however, crystallization in the garnet structure could not be realized.[24] Control over both the stoichiometry and structure is critical in the development of crystalline solid electrolytes as Li-ion transport is governed by the carrier type (defect chemistry), diffusion pathway (anion arrangement), and diffusion type (interstitial direct hopping, interstitial knock-off, and vacancy direct hopping).[40]

An interesting family of solid electrolyte materials is the lithium aluminosilicate ($Li_xAl_xSi_{1-x}O_4$, $0 < x \leq 1$, LASO) system that has several crystal structures (Table S1 in the Supporting Information). In particular, the *β*-eucryptite structure has a framework of *β*-quartz (pure SiO_2), with Li and Al incorporated. *β*-quartz, a hexagonal system (space group $P6_221$ or $P6_421$), is formed by building blocks of SiO_4 tetrahedra with each corner O atom bonded to two tetrahedra, also referred to as bridging oxygen (BO). When Li_2O is added to form lithium-containing silicate glasses $(Li_2O)_x(SiO_2)_{1-x}$, the incorporation of alkali disrupts the SiO_4 tetrahedral network and results in the formation of non-BO (NBO) sites.[41−43] The NBOs provide relatively weak connections between one tetrahedral cation (Si) and one or more Li^+.[42,44] When quartz is doped by Al_2O_3, Al atoms replace Si atoms in the lattice sites because of their comparable atomic sizes. If there are alkali ions present to balance the charge, such as Li^+, the quartz structure changes from SiO_4 tetrahedra and BOs to SiO_4 and AlO_4 tetrahedra and BOs with Li-ions occupying interstitial sites.[43] Ideally, more Li ions are desired for a higher ionic conductivity of the material; hence, incorporation of more Al atoms is needed. However, the oxygen bridge between two Al-ions is unstable due to the Pauling electrostatic valence rule, suggesting that no more than 50% of the Si atoms in tetrahedra can be replaced by Al atoms.[44] *β*-$LiAlSiO_4$ has 50% Si atoms substituted by Al atoms, forming a quartzlike framework of alternating SiO_4 and AlO_4 tetrahedra with Li-ions in the interstitial sites forming 1-D channels parallel to the c axis. $LiAlSiO_4$ exhibits moderate ionic conductivities in the crystalline, glass, and glass ceramic phases at room temperature,[45−48] is electronically insulating, and has an activation energy for ion motion in the range of 0.77−0.95 eV.[9] Because of the 1-D channels along the c axis, the ionic conductivity along the c axis is higher than that in other directions.[45,49] In addition, the ionic conductivity of *β*-$LiAlSiO_4$ has been shown to increase with decreasing film thickness,[48] ideal for microbatteries where the thin-film electrolytes are in the

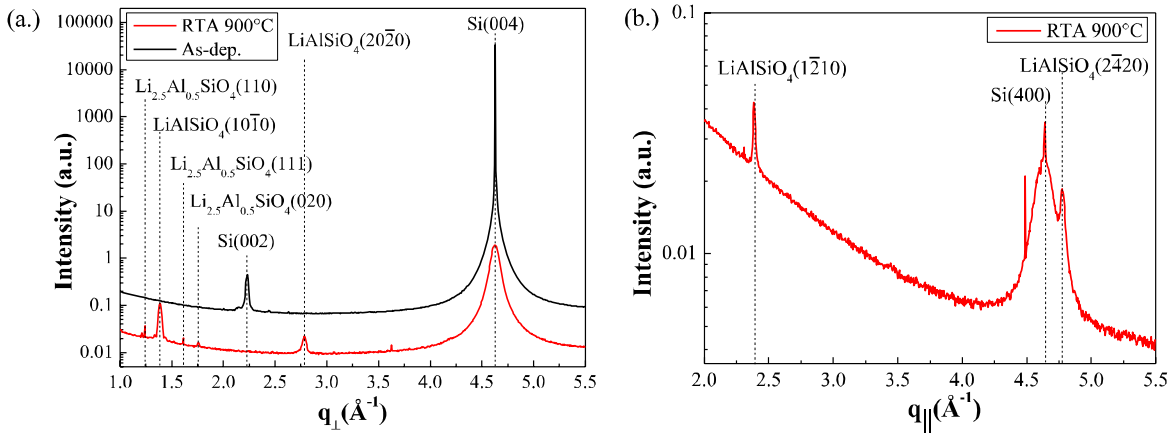

Figure 2. (a) Specular XRD scans of a $Li_xAl_ySi_zO$ sample deposited with an ALD cycle sequence of [12(Al_2O_3)-4(LiOH)-4(SiO_2)]x5, rapid thermal annealed at 900 °C. Peaks corresponding to the reflections of the (10$\bar{1}$0) and (20$\bar{2}$0) planes of the β-eucryptite LiAlSiO4 were observed. (b) In-plane XRD scan where peaks corresponding to the $LiAlSiO_4$(1$\bar{2}$10), Si(400), and $LiAlSiO_4$(2$\bar{4}$20) reflections were observed.

order of nanometers. If the 1-D channels can be aligned in the direction normal to the two electrode surfaces in a thin-film battery structure, enhanced ion transport is expected. Beyond the scope of microbatteries, a electrochemically stable thin-film electrolyte may be viable to improve interfacial properties in solid-state batteries.[5,50]

While ALD has been employed successfully to synthesize amorphous $LiAlSiO_4$,[19] this work focuses on realizing epitaxial and crystalline LASO thin films. To achieve this goal, it is necessary to carefully manage the composition and atomic arrangement by controlling the ALD cycles precisely. An amorphous thin film with the appropriate stoichiometry and atomic arrangement can be converted into a crystalline thin film by a postdeposition thermal treatment. In this work, two types of thermal annealing up to 900 °C were used to control the structural change of lithium aluminum silicate.

RESULTS AND DISCUSSION

The ALD of $Li_xAl_ySi_zO$ thin films was performed through a supercycle process consisting of *a*(TMA-H_2O)-*b*(LiO^{t}Bu-H_2O)-*c*(TEOS-H_2O), where *a,b,c* can be modulated to tune the composition in the deposited films. The ALD growth rates for Al_2O_3 and LiOH were 1.4 and 1.0 Å/cycle, similar to as demonstrated in previous work.[19] SiO_2 incorporation was performed via a tetraethyl orthosilicate (TEOS)/H_2O precursor couple, which has been shown to be reactive in the presence of an electropositive metal atom (Al, Li), through lowering the barrier to reaction of the silicon ethoxy bond to cleavage via H_2O.[51,52] Since the reaction of TEOS/H_2O depends on the presence of other metal cations, the amount of silicon incorporation may be limited as the reactivity is diminished with the increasing number of consecutive TEOS/H_2O cycles.[52] A growth rate for SiO_2 is not reported here due to the inability to quantify it without the presence of another metal oxide, where the effects of each binary ALD process on each other cannot be delineated.

Various $Li_xAl_ySi_zO$ thin films were deposited by altering the *a,b,c* constants in the supercycle and their corresponding surface composition characterized utilizing X-ray photoelectron spectroscopy (XPS) for samples in the as-deposited state and after rapid thermal annealing (RTA) at 900 °C. A RTA approach was taken due to the observation of surface lithium depletion during annealing in an in-situ ultraviolet photoemission spectroscopy (UPS) set-up as shown in Figure S1, which could be due to an alloying reaction of Li at the Si substrate interface or LiOH evaporation. Because of the difficulty in predicting the growth rate of each ALD super cycle, the total number of ALD cycles was held constant instead of the film thickness.

The composition of several samples deposited with various ALD cycle ratios is shown in Figure 1d, where the ALD sequence of 12(Al_2O_3)-4(LiOH)-4(SiO_2) led to a composition closest to the desired $LiAlSiO_4$ stoichiometry. As has been observed in the synthesis of other complex metal oxides via ALD, there was not a clear linear trend between the percentage of each constituent ALD cycle in the overall ALD supercycle and the corresponding incorporation of that metal cation into the film. Thus, in the ALD super cycle, *a*(Al_2O_3)-*b*(LiOH)-*c*(LiOH), the effect of changing *a*, was not independent of *b* and *c*. This most likely is a result of various incubation times as well as varying surface reactive sites dependent on the ALD sequence. For the LiOH component, there was an observed lithium cation content increase with increasing the LiOH ALD cycle percentage, but trends associated with Al_2O_3 and SiO_2 were found to be more complex. Furthermore, because of the low atomic sensitivity factor for Li 1s, an error in peak fitting will produce more pronounced changes in the calculation of relative composition. XPS spectra of the as-deposited and rapid thermal annealed thin film deposited with five supercycles of the ALD sequence of 12(Al_2O_3)-4(LiOH)-4(SiO_2) are shown in Figure 1. Analysis of the XPS spectra was quantified utilizing a single peak for each metal elemental orbital ($2p_{3/2}$ and $2p_{1/2}$ cannot be resolved for Si 2p and Al 2p), where the atomic sensitivity factors (Li: 0.025, Al: 0.193, and Si: 0.328) vary for each element orbital. The binding energy correction was made by setting the C 1s peak associated with sp^3 carbon to 284.8 eV. In the annealed sample, the Al 2p was found to be at 74.6 eV, Li 1s at 56.0 eV, and Si 2p at 102.5 eV, each corresponding to what would be expected for their respective oxides. The composition determined via XPS was $Li_{0.11}Al_{0.09}Si_{0.11}O_{0.24}C_{0.24}$, with a specific ratio of $Li_{0.35}Al_{0.29}Si_{0.36}$, close to the desired $LiAlSiO_4$ stoichiometry. The Li/Al/Si ratio was reproducible within 5% for each metal oxide constituent utilizing the same ALD cycle ratio. Because of the ex-situ nature of the XPS measurements, most of the carbon signal is attributed to adventitious carbon. As can be seen by the high-resolution XPS

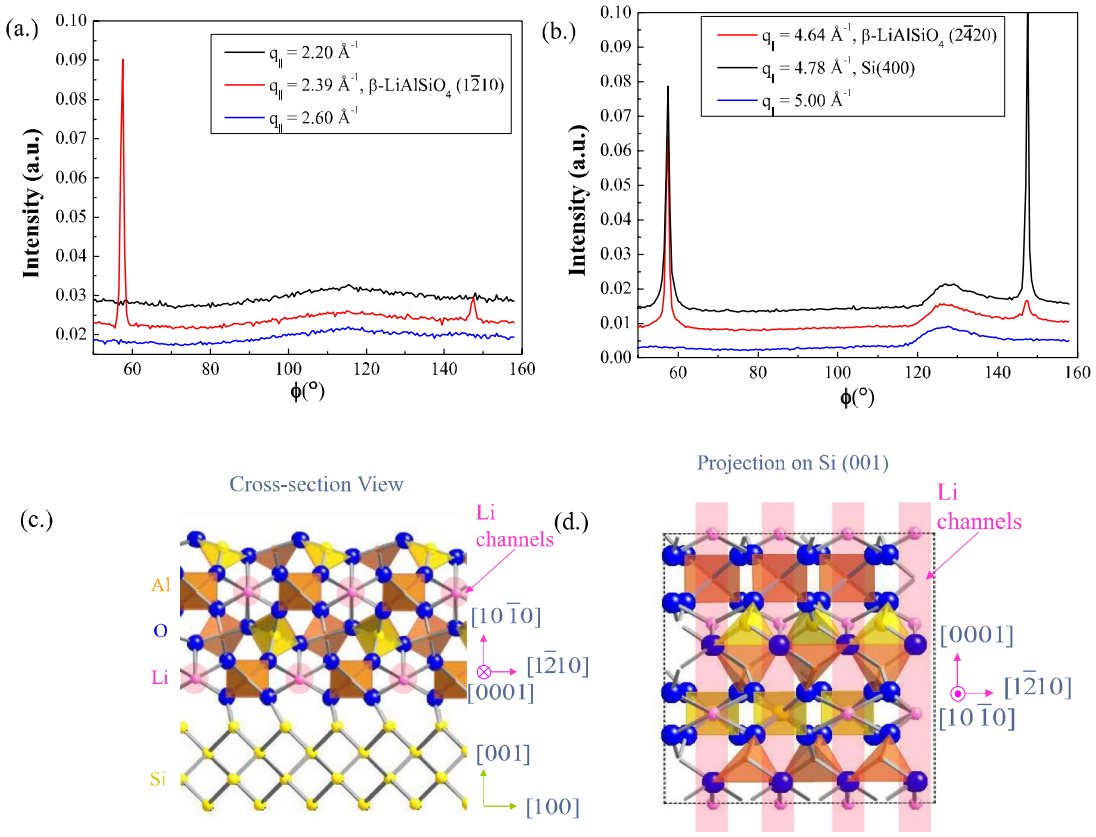

Figure 3. Phi scans of the (a) β-$LiAlSiO_4$ (1$\bar{2}$10) peak and of the (b) Si(400) and $LiAlSiO_4$(2$\bar{4}$20) with q values of 4.74 and 4.64 $Å^{-1}$, respectively, all demonstrating four-fold symmetry. Crystal models showing the interfacial epitaxial relationship of β-$LiAlSiO_4$ on a Si (001) substrate: (c) side-view and (d) top-view. Light pink circles and bars are visual guides to show the location and direction of the 1-D channels.

scans taken over the C 1s binding regions, the as-deposited films had a large peak centered at 290 eV attributed to surface lithium carbonate, which was then subsequently reduced during the RTA treatment. Surface enrichment of lithium was observed to be more prevalent with increasing film thickness in the as-deposited samples similar to that observed previously in the synthesis of $Li_xTi_yO_z$ thin films by ALD.[30] Lithium carbonate, in the presence of metal oxides, has been observed to undergo a reaction at elevated temperatures to release CO_2 to form lithium metal oxides.[53,54] This was further confirmed with angle-resolved XPS of the rapid thermal annealed sample as shown in Figure S2, where an increase in the relative composition of carbon was observed as the take-off angle was reduced from 90 to 30°, corresponding to an increasingly shallow depth probed via XPS. Upon inspection of the relationship among the metal cations (Li, Al, and Si), it was observed that the lithium content increased toward the samples' surface, whereas the aluminum and silicon content decreased uniformly toward the surface.

Initial characterization of the post annealed $Li_xAl_ySi_zO$ thin films was performed utilizing X-ray diffraction (XRD). Of the various $Li_xAl_ySi_zO$ samples deposited, the sample with the closest composition to the $LiAlSiO_4$ stoichiometry deposited with a sequence of 12(Al_2O_3)-4(LiOH)-4(SiO_2) showed diffraction peaks associated with the β-eucryptite phase of $LiAlSiO_4$ at 19.4° and 39.3° associated with reflections of the (10$\bar{1}$0) and (20$\bar{2}$0) planes as shown in Figure S2. To further assess the crystal structure, the 12(Al_2O_3)-4(LiOH)-4(SiO_2) sample was analyzed via XRD at the 10−2 Beamline at the Stanford Synchrotron Radiation Lightsource (SSRL) at SLAC to assess the epitaxial relationship of the $LiAlSiO_4$ thin film with respect to the silicon substrate via specular out-of-plane, radial in-plane, and various phi scans, where the experimental set-up is shown in Table S2.

As can be seen in specular scans shown in Figure 2a, the only reflections observed for the as-deposited film are from the Si(004) plane as well as one centered at 2.23 $Å^{-1}$, which is most likely the "forbidden" Si(002) reflection. After RTA at 900 °C, several peaks can be observed with the most prominent peaks at 1.39 and 2.78 $Å^{-1}$, corresponding to the reflections of the (10$\bar{1}$0) and (20$\bar{2}$0) planes of the β-eucryptite structure. The corresponding d value for the (10$\bar{1}$0) plane was 4.52 Å, slightly less than the literature value of 4.55 Å (JCPDS 01−077-0158), indicating compression in the direction normal to the surface. There were also weaker intensity peaks observed at 1.24, 1.61, and 1.76 $Å^{-1}$, which were identified as the (110), (111), and (020) of the α-$Li_{4-3x}Al_xSiO_4$ phase as reported by Smith et al.,[55] which can be described as an Al-doped Li_4SiO_4 structure.

In-plane scans of the rapid thermal annealed 12(Al_2O_3)-4(LiOH)-4(SiO_2) thin film were also taken to determine the orientation of the crystalline film with regard to the substrate. As can be seen in Figure 2b, peaks were observed at q = 2.39, 4.64, and 4.78 $Å^{-1}$, corresponding to the $LiAlSiO_4$(1$\bar{2}$10), Si(400), and $LiAlSiO_4$(2$\bar{4}$20) reflections. There was an additional sharp peak at q = 4.49 $Å^{-1}$ that is most likely a signature of some unknown impurity. The corresponding d value for the (1$\bar{2}$10) plane was 2.63 Å, slightly larger than the

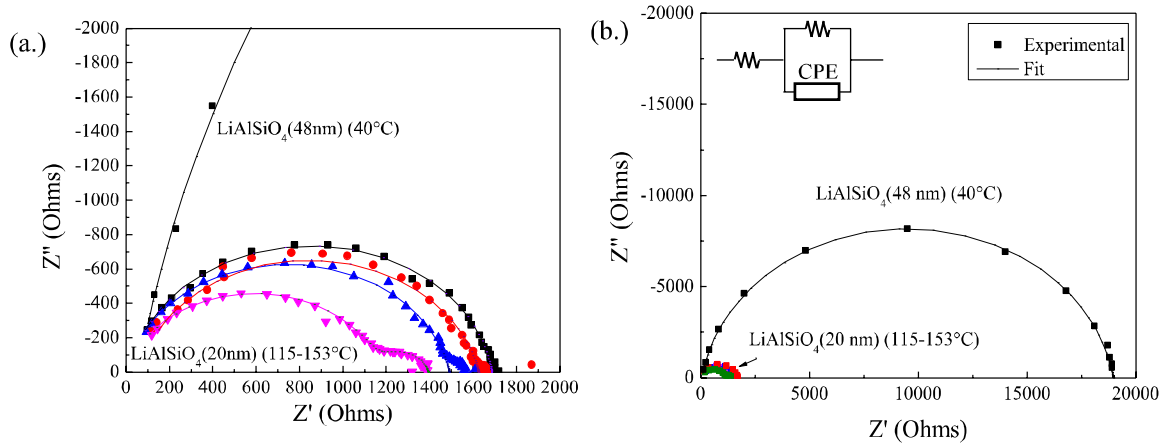

Figure 4. EIS spectra of two $LiAlSiO_4$ samples deposited with a cycle sequence 12(Al_2O_3)-4(LiOH)-4(SiO_2) with thicknesses of 20 and 48 nm corresponding to five and 12 super cycles. The EIS spectra of the 20 nm samples were measured at various temperatures: 115 °C (black), 121 °C (red), 134 °C (blue), and 153 °C (pink). Each EIS spectrum was fit with an equivalent circuit model consisting of a resistor in series with a resistor and constant phase element in parallel. Part (a) and (b) present the same data but at different scales in order to illustrate the trends of both samples.

literature value of 2.62 Å (JCPDS 01−077-0158), indicating slight expansion of the unit cell. An estimate of the grain size was determined via the Scherrer equation, where the full-width at half-max was determined utilizing a pure Gaussian fit of both the $LiAlSiO_4(20\bar{2}0)$ and $LiAlSiO_4(1\bar{2}10)$, and the shape factor (b) was assumed to be 0.9. For the out-of-plane peak, the grain size estimate was calculated at 14.4 nm, whereas the in-plane peak was found to correspond to a grain size estimate of 26.1 nm for the 20−21 nm thin film. No peaks corresponding to the α-$Li_{4-3x}Al_xSiO_4$ were observed in the in-plane XRD measurements.

Further analysis was performed utilizing a phi scan around several of the observed reflections in the in-plane direction to assess the epitaxial relation. First, a phi scan was measured at q = 2.39 $Å^{-1}$ corresponding to the $LiAlSiO_4(1\bar{2}10)$ plane as well as at q values lower and higher in value (q = 2.20 and 2.60 $Å^{-1}$), where two peaks separated by 90° were only observed for the q = 2.39 $Å^{-1}$ scan although a two-fold symmetry is expected for the $(1\bar{2}10)$ plane as shown in Figure 3a. Furthermore, a phi scan was also taken at q = 4.64, 4.78, 5.00 $Å^{-1}$, where the symmetry of the Si(400) and β-$LiAlSiO_4(2\bar{4}20)$ could be assessed. Both the Si(400) and $LiAlSiO_4(2\bar{4}20)$ peaks demonstrated four-fold symmetry (90°) separation, whereas two-fold symmetry was expected for $LiAlSiO_4(2\bar{4}20)$ as shown in Figure 3b. The observed four-fold symmetry for both the $LiAlSiO_4(1\bar{2}10)$ and $LiAlSiO_4(2\bar{4}20)$ planes indicated the presence of twinned structures. Additionally, the peak intensity for the $LiAlSiO_4(2\bar{4}20)$ peak rotated by 90° was much weaker in intensity, which could be due to a slight miscut in the Si(001) substrate. The epitaxial relationship of the crystalline β-$LiAlSiO_4$ to the silicon substrate was determined to be β-$LiAlSiO_4$ $(1\bar{2}10)$||Si (100) and β-$LiAlSiO_4$ $(10\bar{1}0)$||Si (001) as shown in Figure 3c and Figure 3d. It would be ideal for the c axis to be normal to the Si(001) for thin-film battery applications, which would orient the ion-conduction pathways normal to the electrode surface, but alternate substrate selection may produce the desired orientation.

Next, the ionic conductivity of the β-$LiAlSiO_4$ solid electrolyte was characterized by electrochemical impedance spectroscopy (EIS). Doped Si(001) substrates with a resistivity of 0.003−0.005 Ohms-cm were utilized as the substrate for EIS measurements. Characterization of the crystallization of $LiAlSiO_4$ thin films on alternative substrates was beyond the scope of this study, but choice based on lattice match and thermal expansion coefficients may produce more optimal film and interfacial properties. Si was chosen as the substrate in part because of convenience, but it should be noted that it is a high capacity alloying anode utilized for lithium-ion batteries.

EIS spectra were taken at several temperatures as shown in Figure 4a,b for the rapid thermal annealed β-$LiAlSiO_4$ with a thickness of ∼20 nm. The EIS spectra were fit with an equivalent circuit model consisting of a resistor (R_1) in series with a resistor (R_2) and constant phase element (C_1) in parallel. At higher temperatures, a second semicircle with a lower resistance value was observed at lower frequency, and the spectra were fit with an additional constant phase element and resistor in parallel. This signature could be due to slight oxidation of the top Cu electrodes at elevated temperatures. Most importantly, the larger semicircle, which is characteristic of ionic transport in the β-$LiAlSiO_4$ layer, was shown to decrease in diameter with increased temperature because of lower impedance. An Arrhenius plot ($Log(\sigma_{ionic})$ vs 1000/T) is shown in Figure S4, which was roughly linear over the temperatures tested with an activation energy calculated to be 0.18 eV as compared to 0.69−0.84 eV as reported by Shin-ichi et al.[9] for thin films deposited by pulsed laser deposition and 0.7−0.84 eV reported for amorphous ALD $Li_xAl_ySiO_z$ thin films.[19,52] The markedly lower activation energy most likely is due to some more complex phenomenon because of interaction from the Si substrate and the $LiAlSiO_4$ thin film at elevated temperature. One potential cause could be the transition from an ordered to more disordered structure upon heating of the sample, causing a reduction in the ionic conductivity of the $LiAlSiO_4$ layer. Additionally, lithium can alloy with silicon having the potential for there to be an interfacial reaction layer near the substrate and $LiAlSiO_4$ interface, which may be a masking signature of the ionic transport of the $LiAlSiO_4$ layer at elevated temperatures. This could have the effect of increased resistance from the interfacial layer as well as a decrease of the ionic conductivity of the $LiAlSiO_4$ as it is delithiated. A more complex model with an

additional constant phase element in parallel with a resistor can be fit to the data, where the capacitance of the two layers would need to be in the same order of magnitude and the resistance of the interfacial layer would be expected to counteract the reduced resistance associated with the ion transport at higher temperatures in the $LiAlSiO_4$ layer.

A thicker film consisting of 12 supercycles of the $12(Al_2O_3)$-$4(LiOH)$-$4(SiO_2)$ deposited on p-Si was also characterized by impedance spectroscopy as shown in Figure 4a,b. The fitted values correspond to an ionic conductivity of 1.3×10^{-7} S/cm, similar to the extrapolated value for the thinner $LiAlSiO_4$ sample. The extrapolated room temperature ionic conductivity was in the order of 1.2×10^{-7} S/cm, the same order of magnitude of LIPON-based solid electrolytes synthesized via ALD.[14,20] In comparison to past results on amorphous ALD $Li_xAl_ySi_zO_4$ thin films with a similar composition ($Li_{0.40}Al_{0.32}Si_{0.28}O$), the ionic conductivity was found to be ~2 orders of magnitude higher.[52] The resistance increase associated with the thicker film as compared to the thinner 21 nm gives evidence that the measured values are a function of the film thickness, rather than surface effects. Ultimately, a conducting, Li-blocking bottom electrode would be more ideal for characterizing the activation energy and ionic conductivity of the $LiAlSiO_4$ thin films. Furthermore, as the β-$LiAlSiO_4$ thin films tested here are oriented with the c axis perpendicular to the surface, a more ideal orientation may lead to a higher ionic conductivity, as β-$LiAlSiO_4$ is a known 1-D ion conductor with its highest ionic conductivity along the c axis direction.[9,47]

Integration of conformal β-$LiAlSiO_4$ thin films into an all solid-state 3D lithium-ion microbattery does present several processing and material integration challenges. Depending on the integration scheme, the choice of an underlayer with an optimal lattice match and thermal expansion coefficient would lead to most optimized orientation and interface, with the added constraint of the underlayer being a relevant electrode material for lithium-ion microbatteries. Regardless, the films exhibiting optimal ionic conductivity in the specific epitaxial orientation are presented here, where ultimately further process optimization and material integration may lead to further improved performance.

CONCLUSIONS

Structural control of $LiAlSiO_4$ on silicon was demonstrated by RTA following an ALD process where a sequence of b(Al−O)-a(Li−O)-c(Si−O) deposition cycle controls the as-deposited thin-film composition. The crystallization of LASO thin films depends strongly on the as-deposited composition. It was determined that thin films formed by a cycle ratio of (a = 12, b = 4, c = 4) and RTA became epitaxial with respect to the Si(001) substrate, with the relationship of β-$LiAlSiO_4$ $(1\bar{2}10)$‖Si (100) and β-$LiAlSiO_4$ $(10\bar{1}0)$‖Si (001). Thus, the current work represents the first attempt to control the orientation of these 1-D channels in solid-state thin films on silicon. An extrapolated ionic conductivity of 1.2×10^{-7} S/cm was determined for the crystallized β-$LiAlSiO_4$ thin film in which the 1-D Li-ion channels along the c axis of β-$LiAlSiO_4$ were parallel to the substrate. A properly oriented film offers the opportunity to achieve higher ionic conductivities.

EXPERIMENTAL SECTION

The $Li_xAl_ySi_zO$ (LASO) thin films were deposited by thermal ALD on Si(001) coupons (15 × 15 mm) with resistivity 1−5 Ohms-cm and 0.003−0.005 Ohms-cm for impedance measurements. The silicon wafers were not pretreated before deposition and therefore had surface native oxide. The hot wall reactor was operated as described[19] utilizing three organometallic precursors, lithium tert-butoxide (LiO^tBu), trimethylaluminum (TMA), and TEOS, where deionized water was utilized as the oxidant. All depositions consisted of the cycle sequence $a(Al_2O_3)$-$b(LiOH)$-$c(SiO_2)$, where each deposition was chosen to begin with Al_2O_3 deposition because of the high reactivity of the trimethyl aluminum precursor. The deposition temperature for all depositions was 290 °C. LiO^tBu was heated to 140 °C, whereas TEOS and TMA were held at room temperature. Depositions were performed under constant ultrahigh purity N_2 flow at an operating pressure of 120 mTorr. Film thicknesses were quantified via electron microscopy. All the as-deposited films characterized were amorphous as-deposited and stored under ambient conditions.

Synchrotron UPS experiments were carried out at the SSRL (Beamline 8−1 with a photon energy of 140 eV and a pass energy of 29.35 eV) to quantify the composition of LASO. At this photon energy, the cross-section of Li 1s is ~1000 times lager (0.7 Mbarns) compared to XPS, thus providing a higher sensitivity.[56] The synchrotron UPS chamber, possessing the capability of in-situ heating, was used to characterize the surface cation composition in LASO films as well as the change in cation compositions as a function of annealing temperature. It should be noted that the as-deposited samples were stored in ambient conditions for more than 2 weeks prior to measurement. Samples were annealed in-situ for 10−20 min prior to UPS measurement, with varying times associated time needed to reach base pressure in the ultrahigh vacuum chamber.

In addition, postdeposition RTA in N_2 at 900 °C for 60 s was used to crystallize the films while minimizing the Li intercalation (1 min hold 50 °C/s ramp rate). The resulting materials were then characterized by XRD analysis using a photon energy of 13.5 keV at SSRL beamline 10−2 with a four-circle diffractometer and a Pilatus 300 K-W silicon hybrid pixel detector (pixel size 172 μm × 172 μm, sample detector distance 1.1 m). The four-circle diffractometer was used to define the scattering vector q with respect to the thin-film surface normal with four motors, θ, 2θ, φ, and χ, as shown in Table S2 in the Supporting Information. When the sample was oriented horizontally, specular θ−2θ scans were performed to detect peaks corresponding to planes oriented parallel to the sample surface. Peak positions along the 2θ axis were directly correlated to the interplane spacing by Bragg's law. When the sample was oriented vertically, in-plane θ−2θ scans resolve peaks related to planes perpendicular to the surface. In-plane scans with θ and 2θ fixed for particular peaks and varying φ axis allowed the study on symmetry of the peak and the capability of determining an epitaxial relationship between the film and the substrate. Diffraction peaks were then identified by referencing the Joint Committee on Powder Diffraction Standards database.

EIS was performed with a HP4284A LCR meter over a frequency range of 1 MHz to 20 Hz with an input signal of 13 mV. The thin films were characterized on a heated sample stage (Cascade Microtech), where temperatures were monitored by a type-k thermocouple. ALD $Li_xAl_ySi_zO$ films were deposited on conductive Si substrates with resistivity 0.003−.005 Ohms-cm. The thin films were rapid thermal annealed at 900 °C before top-electrode deposition. 500 μm diameter circular electrodes were sputtered through use of a shadow mask consisting of 10 nm Ti and 200 nm of Cu. A portion of the Si coupon was scribed with a diamond scribe; then, a tungsten probe was brought into contact within the scribe mark to make contact with the substrate. Tungsten probes were also utilized to make top contact with the circular Cu pads under light pressure.

AUTHOR INFORMATION

Corresponding Author

Jane P. Chang − *Department of Chemical and Biomolecular Engineering, University of California, Los Angeles, California 90095, United States;* orcid.org/0000-0001-8482-5744; Email: jpchang@ucla.edu

Authors

Ryan Sheil − *Department of Chemical and Biomolecular Engineering, University of California, Los Angeles, California 90095, United States;* orcid.org/0000-0001-6343-7769

Ya-Chuan Perng − *Department of Chemical and Biomolecular Engineering, University of California, Los Angeles, California 90095, United States*

Julian Mars − *SSRL Materials Science Division, SLAC National Accelerator Laboratory, Menlo Park, California 94025, United States;* orcid.org/0000-0003-0557-2983

Jea Cho − *Department of Chemical and Biomolecular Engineering, University of California, Los Angeles, California 90095, United States*

Bruce Dunn − *Department of Material Science and Engineering, University of California, Los Angeles, California 90095, United States;* orcid.org/0000-0001-5669-4740

Michael F. Toney − *SSRL Materials Science Division, SLAC National Accelerator Laboratory, Menlo Park, California 94025, United States;* orcid.org/0000-0002-7513-1166

Author Contributions

[‖]R.S. and Y.-C.P. authors contributed equally. The manuscript was written through contributions of all authors. All authors have given approval to the final version of the manuscript.

Funding

The authors acknowledge the funding support from the National Science Foundation (DMR − 0932761) and the Office of Naval Research (N00014-13-1-0466).

Notes

The authors declare no competing financial interest.

ACKNOWLEDGMENTS

The authors thank Danielle Butts, Chris Choi, and Grace Whang for insightful discussions and helping with initial electrochemical characterization. The authors would also like to thank the Nanoelectronics Research Facility (NRF), acknowledge the use of the Integrated Systems Nanofabrication Cleanroom (ISNC) at the California NanoSystems Institute (CNSI) in UCLA. Portions of this research were carried out at the SSRL, a national user facility operated by Stanford University on behalf of the U.S. Department of Energy, Office of Basic Energy Sciences.

REFERENCES

(1) Shit, R. C.; Sharma, S.; Puthal, D.; Zomaya, A. Y. Location of Things (LoT): A Review and Taxonomy of Sensors Localization in IoT Infrastructure. *IEEE Commun. Surv. & Tutorials* **2018**, *20*, 2028−2061.

(2) Long, J. W.; Dunn, B.; Rolison, D. R.; White, H. S. Three-Dimensional Battery Architectures. *Chem. Rev.* **2004**, *104*, 4463−4492.

(3) Arthur, T. S.; Bates, D. J.; Cirigliano, N.; Johnson, D. C.; Malati, P.; Mosby, J. M.; Perre, E.; Rawls, M. T.; Prieto, A. L.; Dunn, B. Three-dimensional electrodes and battery architectures. *MRS Bull.* **2011**, *36*, 523−531.

(4) Zhao, Y.; Zheng, K.; Sun, X. Addressing Interfacial Issues in Liquid-Based and Solid-State Batteries by Atomic and Molecular Layer Deposition. *Joule* **2018**, *2*, 2583−2604.

(5) Liu, J.; Zhu, H.; Shiraz, M. H. A. Toward 3D Solid-State Batteries via Atomic Layer Deposition Approach. *Front. in Energy Res.* **2018**, *6*, No. 00010.

(6) Pearse, A.; Schmitt, T.; Sahadeo, E.; Stewart, D. M.; Kozen, A.; Gerasopoulos, K.; Talin, A. A.; Lee, S. B.; Rubloff, G. W.; Gregorczyk, K. E. Three-Dimensional Solid-State Lithium-Ion Batteries Fabricated by Conformal Vapor-Phase Chemistry. *ACS Nano* **2018**, *12*, 4286−4294.

(7) Knoops, H.; Donders, M. E.; Baggetto, L.; Van de Sanden, M. C.; Notten, P.; Kessels, W. M. Atomic Layer Deposition for All-Solid-State 3D-Integrated Batteries. *ECS Trans.* **2009**, *25*, 333−344.

(8) Oudenhoven, J. F. M.; Baggetto, L.; Notten, P. H. L. All-Solid-State Lithium-Ion Microbatteries: A Review of Various Three-Dimensional Concepts. *Adv. Energy Mater.* **2011**, *1*, 10−33.

(9) Shin-ichi, F.; Satoshi, S.; Kaduhiro, S.; Hitoshi, T. Preparation and ionic conductivity of β-LiAlSiO4 thin film. *Solid State Ionics* **2004**, *167*, 325−329.

(10) Loho, C.; Djenadic, R.; Bruns, M.; Clemens, O.; Hahn, H. Garnet-Type Li7La3Zr2O12 Solid Electrolyte Thin Films Grown by CO2-Laser Assisted CVD for All-Solid-State Batteries. *J. Electrochem. Soc.* **2017**, *164*, A6131−A6139.

(11) Bitzer, M.; Van Gestel, T.; Uhlenbruck, S.; Hans Peter, B. Sol-gel synthesis of thin solid Li7La3Zr2O12 electrolyte films for Li-ion batteries. *Thin Solid Films* **2016**, *615*, 128−134.

(12) Dudney, N. J.; Jang, Y.-I. Analysis of thin-film lithium batteries with cathodes of 50 nm to 4 μm thick LiCoO2. *J. Power Sources* **2003**, *119-121*, 300−304.

(13) Yu, X.; Bates, J. B.; Jellison, G. E.; Hart, F. X. A Stable Thin-Film Lithium Electrolyte: Lithium Phosphorus Oxynitride. *J. Electrochem. Soc.* **1997**, *144*, 524−532.

(14) Pearse, A. J.; Schmitt, T. E.; Fuller, E. J.; El-Gabaly, F.; Lin, C.-F.; Gerasopoulos, K.; Kozen, A. C.; Talin, A. A.; Rubloff, G.; Gregorczyk, K. E. Nanoscale Solid State Batteries Enabled by Thermal Atomic Layer Deposition of a Lithium Polyphosphazene Solid State Electrolyte. *Chem. Mater.* **2017**, *29*, 3740−3753.

(15) Chen, N.; Reeja-Jayan, B.; Lau, J.; Moni, P.; Liu, A.; Dunn, B.; Gleason, K. K. Nanoscale, conformal polysiloxane thin film electrolytes for three-dimensional battery architectures. *Mater. Horiz.* **2015**, *2*, 309−314.

(16) Dudney, N. J. Thin Film Microbatteries. *Interface* **2008**, 44−48.

(17) Put, B.; Mees, M. J.; Hornsveld, N.; Hollevoet, S.; Sepúlveda, A.; Vereecken, P. M.; Kessels, W. M. M.; Creatore, M. Plasma-Assisted ALD of LiPO(N) for Solid State Batteries. *J. Electrochem. Soc.* **2019**, *166*, A1239−A1242.

(18) Wang, B.; Liu, J.; Sun, Q.; Li, R.; Sham, T.-K.; Sun, X. Atomic layer deposition of lithium phosphates as solid-state electrolytes for all-solid-state microbatteries. *Nanotechnology* **2014**, *25*, 504007.

(19) Perng, Y.-C.; Cho, J.; Sun, S. Y.; Membreno, D.; Cirigliano, N.; Dunn, B.; Chang, J. P. Synthesis of ion conducting LixAlySizO thin films by atomic layer deposition. *J. Mater. Chem. A* **2014**, *2*, 9566−9573.

(20) Kozen, A. C.; Pearse, A. J.; Lin, C.-F.; Noked, M.; Rubloff, G. W. Atomic Layer Deposition of the Solid Electrolyte LiPON. *Chem. Mater.* **2015**, *27*, 5324−5331.

(21) Liu, J.; Banis, M. N.; Li, X.; Lushington, A.; Cai, M.; Li, R.; Sham, T.-K.; Sun, X. Atomic Layer Deposition of Lithium Tantalate Solid-State Electrolytes. *J. Phys. Chem. C* **2013**, *117*, 20260−20267.
(22) Wang, B.; Liu, J.; Norouzi Banis, M.; Sun, Q.; Zhao, Y.; Li, R.; Sham, T.-K.; Sun, X. Atomic Layer Deposited Lithium Silicates as Solid-State Electrolytes for All-Solid-State Batteries. *ACS Appl. Mater. Interfaces* **2017**, *9*, 31786−31793.
(23) Kazyak, E.; Chen, K.-H.; Davis, A. L.; Yu, S.; Sanchez, A. J.; Lasso, J.; Bielinski, A. R.; Thompson, T.; Sakamoto, J.; Siegel, D. J.; Dasgupta, N. P. Atomic layer deposition and first principles modeling of glassy Li3BO3−Li2CO3 electrolytes for solid-state Li metal batteries. *J. Mater. Chem. A* **2018**, *6*, 19425−19437.
(24) Kazyak, E.; Chen, K.-H.; Wood, K. N.; Davis, A. L.; Thompson, T.; Bielinski, A. R.; Sanchez, A. J.; Wang, X.; Wang, C.; Sakamoto, J.; Dasgupta, N. P. Atomic Layer Deposition of the Solid Electrolyte Garnet Li7La3Zr2O12. *Chem. Mater.* **2017**, *29*, 3785−3792.
(25) Shibata, S. Thermal Atomic Layer Deposition of Lithium Phosphorus Oxynitride as a Thin-Film Solid Electrolyte. *J. Electrochem. Soc.* **2016**, *163*, A2555−A2562.
(26) Donders, M. E.; Knoops, H. C. M.; Kessels, W. M. M.; Notten, P. H. L. Co3O4 as anode material for thin film micro-batteries prepared by remote plasma atomic layer deposition. *J. Power Sources* **2012**, *203*, 72−77.
(27) Cao, Y.-Q.; Wang, S.-S.; Liu, C.; Wu, D.; Li, A.-D. Atomic layer deposition of ZnO/TiO2 nanolaminates as ultra-long life anode material for lithium-ion batteries. *Sci. Rep.* **2019**, *9*, 11526.
(28) Xie, M.; Sun, X.; Zhou, C.; Cavanagh, A. S.; Sun, H.; Hu, T.; Wang, G.; Lian, J.; George, S. M. Amorphous Ultrathin TiO2 Atomic Layer Deposition Films on Carbon Nanotubes as Anodes for Lithium Ion Batteries. *J. Electrochem. Soc.* **2015**, *162*, A974−A981.
(29) Ahmed, B.; Anjum, D. H.; Gogotsi, Y.; Alshareef, H. N. Atomic layer deposition of SnO2 on MXene for Li-ion battery anodes. *Nano Energy* **2017**, *34*, 249−256.
(30) Miikkulainen, V.; Nilsen, O.; Laitinen, M.; Sajavaara, T.; Fjellvåg, H. Atomic layer deposition of LixTiyOz thin films. *RSC Adv.* **2013**, *3*, 7537−7542.
(31) Stewart, D. M.; Pearse, A. J.; Kim, N. S.; Fuller, E. J.; Talin, A. A.; Gregorczyk, K.; Lee, S. B.; Rubloff, G. W. Tin Oxynitride Anodes by Atomic Layer Deposition for Solid-State Batteries. *Chem. Mater.* **2018**, *30*, 2526−2534.
(32) Donders, M. E.; Arnoldbik, W. M.; Knoops, H. C. M.; Kessels, W. M. M.; Notten, P. H. L. Atomic Layer Deposition of LiCoO2 Thin-Film Electrodes for All-Solid-State Li-Ion Micro-Batteries. *J. Electrochem. Soc.* **2013**, *160*, A3066−A3071.
(33) Mattelaer, F.; Geryl, K.; Rampelberg, G.; Dendooven, J.; Detavernier, C. Amorphous and Crystalline Vanadium Oxides as High-Energy and High-Power Cathodes for Three-Dimensional Thin-Film Lithium Ion Batteries. *ACS Appl. Mater. Interfaces* **2017**, *9*, 13121−13131.
(34) Dobbelaere, T.; Mattelaer, F.; Dendooven, J.; Vereecken, P.; Detavernier, C. Plasma-Enhanced Atomic Layer Deposition of Iron Phosphate as a Positive Electrode for 3D Lithium-Ion Microbatteries. *Chem. Mater.* **2016**, *28*, 3435−3445.
(35) Miikkulainen, V.; Ruud, A.; OØstreng, E.; Nilsen, O.; Laitinen, M.; Sajavaara, T.; Fjellvåg, H. Atomic Layer Deposition of Spinel Lithium Manganese Oxide by Film-Body-Controlled Lithium Incorporation for Thin-Film Lithium-Ion Batteries. *J. Phys. Chem. C* **2013**, *118*, 1258−1268.
(36) Gregorczyk, K.; Henn-Lecordier, L.; Gatineau, J.; Dussarrat, C.; Rubloff, G. Atomic Layer Deposition of Ruthenium Using the Novel Precursor bis(2,6,6-trimethyl-cyclohexadienyl)ruthenium. *Chem. Mater.* **2011**, *23*, 2650−2656.
(37) Aaltonen, T.; Ritala, M.; Sajavaara, T.; Keinonen, J.; Leskelä, M. Atomic Layer Deposition of Platinum Thin Films. *Chem. Mater.* **2003**, *15*, 1924−1928.
(38) Väyrynen, K.; Mizohata, K.; Räisänen, J.; Peeters, D.; Devi, A.; Ritala, M.; Leskelä, M. Low-Temperature Atomic Layer Deposition of Low-Resistivity Copper Thin Films Using Cu(dmap)2 and Tertiary Butyl Hydrazine. *Chem. Mater.* **2017**, *29*, 6502−6510.
(39) Blakeney, K. J.; Winter, C. H. Atomic Layer Deposition of Aluminum Metal Films Using a Thermally Stable Aluminum Hydride Reducing Agent. *Chem. Mater.* **2018**, *30*, 1844−1848.
(40) Zhang, B.; Tan, R.; Yang, L.; Zheng, J.; Zhang, K.; Mo, S.; Lin, Z.; Pan, F. Mechanisms and properties of ion-transport in inorganic solid electrolytes. *Energy Storage Mater.* **2018**, *10*, 139−159.
(41) Lammert, H.; Kunow, M.; Heuer, A. Complete Identification of Alkali Sites in Ion Conducting Lithium Silicate Glasses: A Computer Study of Ion Dynamics. *Phys. Rev. Lett.* **2003**, *90*, 215901.
(42) Soltay, L. G.; Henderson, G. S. The Structure Of Lithium-Containing Silicate And Germanate Glasses. *The Canad. Mineral.* **2005**, *43*, 1643−1651.
(43) Stebbins, J. F.; Xu, Z. NMR evidence for excess non-bridging oxygen in an aluminosilicate glass. *Nature* **1997**, *390*, 60−62.
(44) Loewenstein, W. The distribution of aluminum in the tetrahedra of silicates and aluminates. *Am. Mineral.* **1954**, *39*, 92−96.
(45) Nagel, W.; Böhm, H. Ionic conductivity studies on LiAlSiO4—SiO2 solid solutions of the high quartz type. *Solid State Commun.* **1982**, *42*, 625−631.
(46) Alpen, U. V.; Schönherr, E.; Schulz, H.; Talat, G. H. β-eucryptite—a one-dimensional Li-ionic conductor. *Electrochim. Acta* **1977**, *22*, 805−807.
(47) Thangadurai, V.; Weppner, W. Solid state lithium ion conductors: Design considerations by thermodynamic approach. *Ionics* **2002**, *8*, 281−292.
(48) Furusawa, S.-i.; Tabuchi, H.; Tsurui, T. Ionic conductivity of lithium alumino-silicate thin films on SiO2 glass and Al2O3 substrates. *Solid State Ionics* **2007**, *178*, 1033−1038.
(49) Alekseeva, I.; Dymshits, O.; Ermakov, V.; Zhilin, A.; Petrov, V.; Tsenter, M. Raman spectroscopy quantifying the composition of stuffed β-quartz derivative phases in lithium aluminosilicate glass-ceramics. *J. Non-Cryst. Solids* **2008**, *354*, 4932−4939.
(50) Vinado, C.; Wang, S.; He, Y.; Xiao, X.; Li, Y.; Wang, C.; Yang, J. Electrochemical and interfacial behavior of all solid state batteries using Li10SnP2S12 solid electrolyte. *J. Power Sources* **2018**, *396*, 824−830.
(51) Cho, J.; Kim, T.; Seegmiller, T.; Chang, J. P. Mechanistic study of atomic layer deposition of AlxSiyO thin film via in-situ FTIR spectroscopy. *J. Vacuum Sci. & Technol. A* **2015**, *33*, No. 05E130.
(52) Cho, J.; Kim, T.; Seegmiller, T.; Chang, J. P. Elucidating the Surface Reaction Mechanisms During Atomic Layer Deposition of LixAlySizO by in Situ Fourier Transform Infrared Spectroscopy. *J. Phys. Chem. C* **2016**, *120*, 11837−11846.
(53) Mäntymäki, M.; Atosuo, E.; Heikkilä, M. J.; Vehkamäki, M.; Mattinen, M.; Mizohata, K.; Räisänen, J.; Ritala, M.; Leskelä, M. Studies on solid state reactions of atomic layer deposited thin films of lithium carbonate with hafnia and zirconia. *J. Vacuum Sci. & Technol. A* **2019**, *37*, No. 020929.
(54) Atosuo, E.; Mäntymäki, M.; Mizohata, K.; Heikkilä, M. J.; Räisänen, J.; Ritala, M.; Leskelä, M. Preparation of Lithium Containing Oxides by the Solid State Reaction of Atomic Layer Deposited Thin Films. *Chem. Mater.* **2017**, *29*, 998−1005.
(55) Smith, R. I.; West, A. R. Crystal structure of α-Li2.5Al0.5SiO4. *J. Solid State Chem.* **1991**, *93*, 436−442.
(56) Yeh, J. J.; Lindau, I. Atomic subshell photoionization cross sections and asymmetry parameters: $1 \leqslant Z \leqslant 103$. *At. Data Nucl. Data Tables* **1985**, *32*, 1−155.